Russian Geology and Geophysics
Vol. 44, No. 6, pp. 566-586, 2003

Geologiya i Geofizika
UDC 551.24

THREE-DIMENSIONAL VELOCITY STRUCTURE OF UPPER MANTLE BENEATH THE ALPINE-HIMALAYAN OROGEN

I.Yu. Kulakov, S.A. Tychkov, N.A. Bushenkova, and A.N. Vasilevsky

Institute of Geology, Siberian Branch of the RAS, 3 prosp. Akad. Koptyuga, Novosibirsk, 630090, Russia

Upper mantle beneath the Alpine-Himalayan orogen (AHO) at depths from 100 to 500 km has been studied using ITS inversion of teleseismic *P* travel times from earthquakes that occurred in the region and were recorded by the worldwide seismological network (ISC bulletins). 3D velocity maps were obtained as a sum of independent inversions in about sixty overlapping blocks 600–1000 km across. This approach is similar to high-frequency spatial filtration and provides a much higher resolution than the global tomography. High-velocity zones within the orogen have been interpreted as signature of continental or oceanic lithosphere sinking to the upper mantle under active regional compression. The maps show well pronounced traces of subduction in the regions of Cretan arc, Hindukush, and Burma, also confirmed by independent data, as well as other less certain evidence of subduction. Positive anomalies in the western part of the orogen are attributed to subduction in the area of Cyprus and along the Caucasus—Kopet Dagh—Lut belt. The lithosphere of the Indian plate subducted beneath the Himalayas and Tibet has a rather complicated structure. Zones of sinking lithosphere are traceable around the Tarim block. Distinct low-velocity anomalies in Mongolia, Tibet, and Southern Caspian basin may be produced by active mantle plumes.

Three-dimensional velocity structure, upper mantle, collision, subduction, plume, Alpine-Himalayan orogen

INTRODUCTION

The Alpine—Himalayan orogen (AHO) makes the southern boundary of the Eurasian plate and separates it from the African plate in Europe, from the Arabian plate in Middle Asia and from the Indian plate in the east. This area of intricate plate interaction has long been a focus of interest for geologists; however, there remains a lot to be investigated as to the structure and evolution of the lithosphere. The generalized lithospheric structure of the orogen based on [1–6] and this study is presented in Fig. 1.

The Alpine—Himalayan orogen is a zone of high seismic activity (Fig. 2). Most events nucleated below 50 km are anyhow associated with contemporary collision processes and are restricted to a narrow belt of Burma—Himalayas—Pamirs—Zagros—Aegean and Sardinian arcs. Sources as deep as 300–400 km (in Apennines, Tyrrhenian Sea, Carpathians, Pamirs, Indo-China, etc.) are concentrated locally at points or nodes. The pattern of deep earthquakes is diagnostic of major subduction zones within the orogen and helps in interpretation of tomography results.

The western segment of the orogen includes the Mediterranean region and Minor Asia largely investigated in terms of tectonics [1, 7, 8]. The tectonism of this region consisting of microplates and numerous fragments of oceanic continental lithosphere is chiefly controlled by the collision of the African plate with Europe. Most of the Mediterranean tectonic structures emerged in late Cenozoic (21–0 Ma): the Alps were produced by a collision of the Apulian plate with Europe in the Miocene (21–15 Ma); the Apennines originated during a collision of the Corsica-Sardinia microplate that moved eastward from the coast of Spain with the western border of the Apulian plate; the Dinarides and Hellenides result from a collision of several blocks with the western Apulian plate. The recent activity has acted as subduction of the oceanic African lithosphere northward under the Cretan and Calabrian

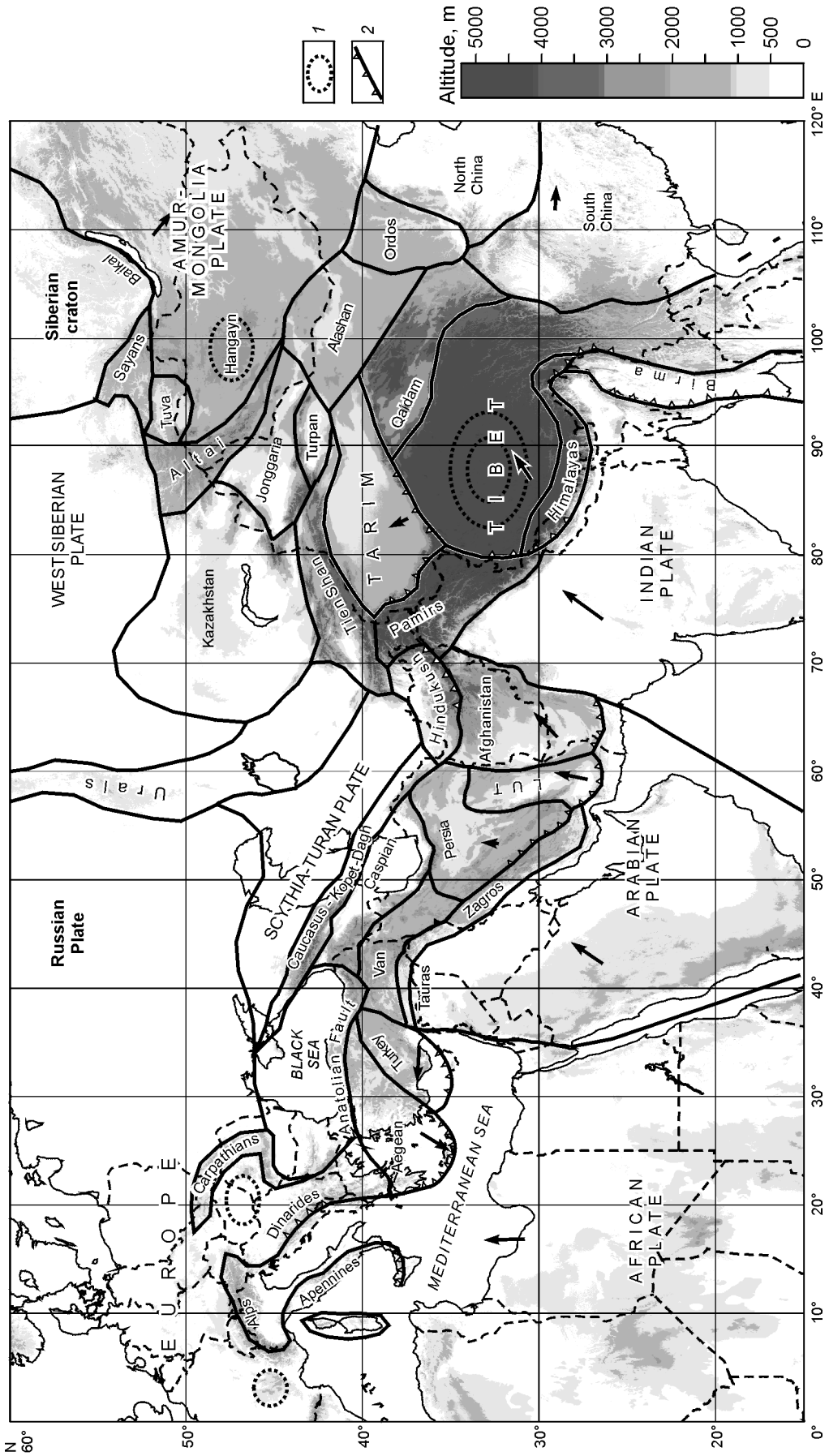

Fig. 1. Surface topography and generalized structure of study territory, from [1–6] and this research. Velocities and directions of plate motion are shown schematically by arrows. 1 mm of arrow length corresponds to ~0.6 mm/year. *1* — location of mantle plumes; *2* — direction of slab sinking.

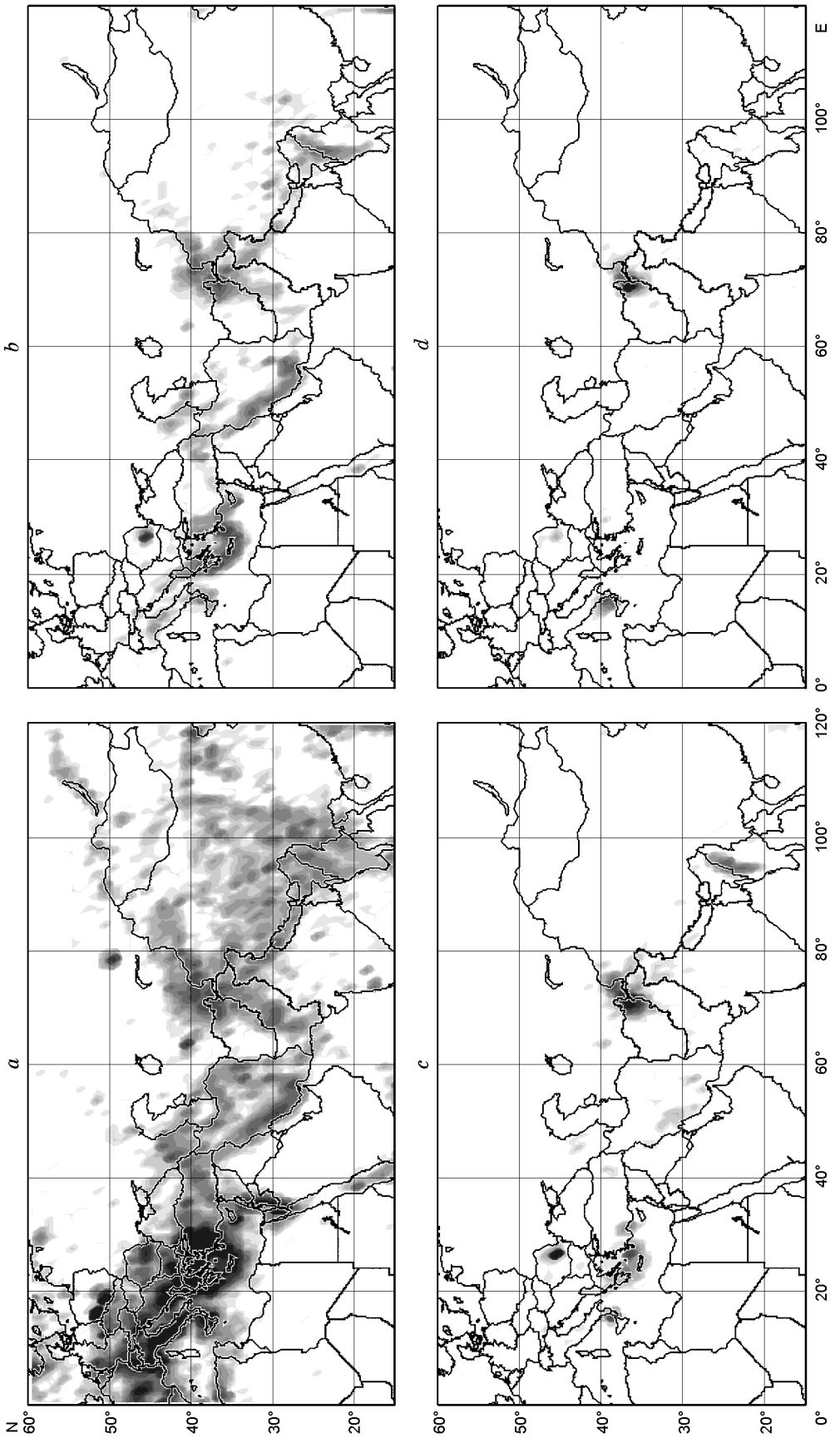

Fig. 2. Distribution of deep seismicity in Alpine-Himalayan orogen at different depth intervals: 0–50 km (*a*), 50–100 km (*b*), 100–200 km (*c*), and below 200 km (*d*). Earthquakes nucleated at 0 to 50 km (top left map) were used for ITS in this research.

arcs, slab detachment beneath the Apennines and the Dinarides, and active volcanism in the Aegean Sea and Western Greece, the Tyrrhenian Sea, and the Pannonian basin, most often attributed to passive spreading or mantle plumes.

The central segment of the orogen from the Caucasus to the Pamirs is a complex mosaic produced in Late Mesozoic and Cenozoic time by amalgamation of several blocks different in nature and age during a collision of Eurasia with Gondwanian microcontinents. Widely distributed ophiolites mark alternation of small continental blocks and Tethys oceanic basins which closed in the Cretaceous [1, 2]. The regional tectonics is controlled by rotation of rigid lithospheric blocks (eight major blocks (Fig. 1) are Indian, Afghanistan, Lut, Persian, Caspian Sea, Black Sea, Turkish and Arabian plates [3]) separated by zones of weakness. A volcanic zone between the plates of Persia, Caspian Sea, Black Sea, Turkey, and Arabia involves at least twelve Quaternary and four modern volcanoes, including world largest Elbourz in Persia, Elbrus in the Caucasus, and Ararat in eastern Turkey. The volcanic activity has been attributed to mantle plumes [9] or to westward compression from the Arabian plate upon the weak material of the Turkish-Iranian plateau [10].

The origin of the Great Caucasus and Kopet Dagh sutures was dated back to Hercynian time [11], but the existence of seismic activity down to a depth of 200 km indicates that the collision is still active. Many other collision zones within this segment of the orogen (Taurus-Zagros suture, Sistan suture in Iran, etc.) were formed in the Cenozoic [12]. However, the geometry of the blocks and collision zones has been so far debated [1–4], and reliable constraining of block boundaries remains a vital problem.

The eastern segment of the AHO from the Pamirs to Indo-China has evolved under a general control from the India/Eurasia collision since 60–50 Ma [13]. However, the lithosphere of the region began to form much earlier, as the Tarim plate collided with the Tien Shan in the late Devonian, over 300 Ma [13], and the Tibet block accreted to Asia in the Triassic-latest Jurassic [15]. The Cenozoic Indian collision rebuilt the block structure over a large territory [5, 16]. The related tectonism acted upon relatively weak lithosphere between rigid blocks. Compression caused lithospheric thickening and orogeny (Himalayan, Hindu Kush, Tien Shan, Nan Shan, Altai, Stanovik) [17]; elsewhere lithospheric blocks moved apart under extension and caused the origin of rifts like Baikal.

An alternative evolution model of the contemporary structure of Central Asia suggests interaction of plates and mantle plumes in which plumes beneath Asia are responsible for the style of microplate rotation and the northward propagation of tectonic activity from Tibet to Siberia [18, 19]. The choice between the two alternatives requires more information on the structure and evolution of the region, including new models of mantle structure and dynamics.

It remains unclear whether the continental lithosphere can be involved in subduction as a result of continental collision. This problem can be investigated due to analysis of slab behavior in the upper mantle imaged by seismic tomography.

In this study we try to detect traces of sinking lithosphere in the upper mantle in collision sutures and low-density zones associated with rising mantle plumes. The knowledge of lithospheric behavior in these zones may shed light on plate interaction and the presence of hot plumes.

SEISMIC TOMOGRAPHY

Seismic tomography, a powerful tool for deep structure studies, has seen much recent progress as a result of improved computing facilities, augmented global seismological data bank, installation of new seismographic stations, advance in data acquisition and processing techniques, etc. Some of new high-resolution global models [20–24] reach a precision of regional modeling, but high-resolution regional modeling of the mantle still has not been achieved over a great portion of the Earth.

The mantle structure beneath the Alpine—Himalayan orogen has been a subject of many studies. Detailed tomographic models for its European and Middle East parts are reported in [25, 26] and agree well with each other and with the global model [24].

Modeling of its other parts, however, remains problematic, in spite of the available mantle models for Hindukush and Pamirs [27, 28], Tibet [29–34], China [35], and southern Siberia and Mongolia [36–38]. Comparison of these models in overlap areas and their correlation to the global model [24] is unsatisfactory, mainly because of data scarcity. The solution may come from alternative tomographic modeling on the basis of new approaches and data.

This research is based on the Inverse Teleseismic Scheme (ITS) developed by Kulakov [37] and implies the use of travel times from sources inside the study region recorded by the worldwide seismological network. ITS is theoretically equivalent to the traditional tomographic scheme based on the reciprocity principle but differs in a number of practical details. In particular, a significantly higher multiplicity of the ITS observation system (number

of sources recorded by a station and number of stations that record an event) allows more reliable computing of anomaly-related travel time residuals. ITS can be applied to any active tectonic region with a sufficient number of earthquakes, as it uses data available from open-file ISC bulletins rather than data from regional networks which are often scarce and of low quality. The scheme has been used for investigation of the upper mantle in southern Siberia [37].

However, ITS is sensible to errors in source location. This problem is considered separately in a section below, and a test is suggested to allow for mislocation effects.

A question arises whether the data of the traditional and the inverse schemes can be combined. This may be difficult in many regions, because of sparse seismographic networks. According to our experience, determination of residuals can be reliable if the causative event is recorded by at least ten stations. For example, teleseismic data from the Altai-Sayan area obtained using the traditional scheme [36] and records from 5 to 12 permanent stations bear noise exceeding the relevant residuals. At the same time, information from regional networks is useful to check source parameters (location and origin time of earthquakes).

INVERSION

The optimum width-to-height ratio for a target volume in teleseismic research is between 1.5 and 2, as larger areas are more strongly subject to lower mantle effects. Therefore, depths down to 500 km can be scanned in a territory with horizontal dimensions within 1000 km. To cover a larger area, we suggest to apply inversion to a number of separate overlapping circular blocks with their centers spaced at distances shorter than their horizontal dimensions (200–300 km for blocks of 1000 km in diameter) to provide the appropriate overlap. The results from the separate blocks are then summarized on a single map (Fig. 3). The final model is computed following

$$dV(x, y, z) = \frac{\sum_{i=1}^{N} dV_i(x, y, z)\, w_i^1(x, y. z)\, w_i^2(x, y, z)}{\sum_{i=1}^{N} w_i^1(x, y, z)\, w_i^2(x, y, z)},$$

where dV_i is the velocity anomaly in the i-th block and w^1 and w^2 are two weight functions. The value of w^1 depends on distance from a point to the center of blocks, and the reliability of results diminishes peripheryward. w^1 is found as

$$w_i^1(x, y, z) = \begin{cases} 1 & r < R/2 \\ 2 - \frac{2r}{R}, & \text{if } R/2 > r > R \\ 0 & r > R \end{cases},$$

where R is the radius of the block, r is the distance from the block center.

The other weight function, w^2, is determined using the same relationships based on the position of the point relative to the parameterization grid. In this case, R is the user-specified maximum distance from the nearest grid node.

A problem in this method it that inversion in each block is made with respect to some average velocity models different in all blocks, so that a “negative” anomaly in one block may be higher than a “positive” anomaly in another. The situation can be illustrated by an example from the everyday life. Suppose we are to take a picture by a digital camera in a room with a window and want to obtain a clear image of details both on the wall and behind the window. A large-scope picture images just a white square of the window against the dark background of the walls, but if we take several close-up pictures slightly moving the camera each time, we can see details both on the walls and behind the window as the average light level (reference model) varies in different images. Although not realistic, the resultant panorama gives more details than the general view of dark walls and a white window.

This example illustrates the difference between global tomographic models and the models obtained as a sum of separate inversions. Our approach allows for high-frequency variations of velocity anomalies (“details on the wall and behind the window”) but is poorly sensitive to large patterns of a size comparable to the study volume (“the window itself”). It may cause serious problems if we address absolute velocities, as in 3D ray tracing in the real Earth. In geodynamic implications, however, variations of physical parameters are important rather than the absolute values. Therefore, the model we suggest can be useful for geological implications.

In contrast to the schemes that employ rays restricted to the upper mantle, the teleseismic scheme is insensitive

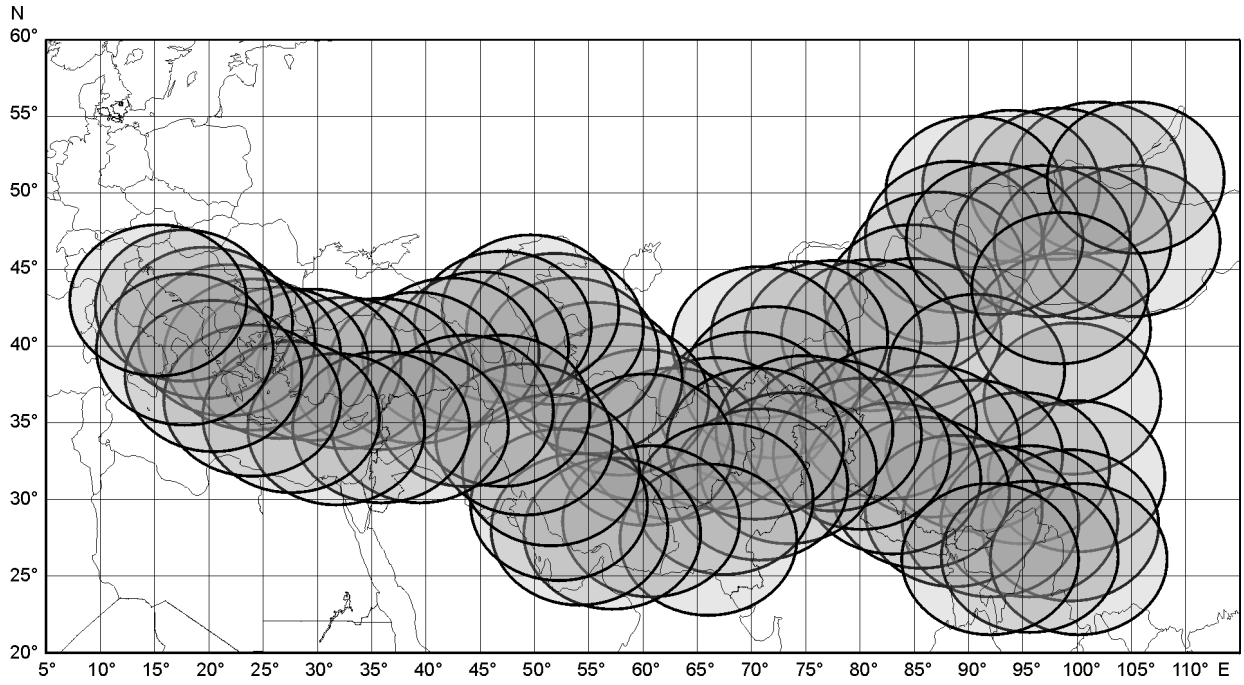

Fig. 3. Position of blocks used for separate inversions followed by averaging.

to upper mantle effects in the reference model. Since rays pass at a very limited range of angles, absolute velocity variations within the studied depth interval cannot cause a significant effect on relative residuals. At the same time, ray paths cannot be disturbed by an error in the reference model in the upper mantle, because the turn point of rays is located in the lower mantle where the velocity distribution is fairly smooth and can be precisely estimated.

Note that ITS requires well scattered areal distribution of sources on the day surface, and is inapplicable to areas like oceanic subduction zones in which earthquakes cluster along narrow belts.

DATA PROCESSING

This research is based on data from ISC bulletins for the period of 1964 to 1996. Data selection, processing, and inversion have been performed separately for sixty overlapping circular blocks that cover the territory of the Alpine-Himalayan orogen (Fig. 3). The upper limit of the target volume has been defined at a depth of 100 km. All effects that disturb travel times above this boundary were allowed for by source correction.

Travel times from earthquakes that occurred within a block and were recorded by the worldwide seismographic network were selected on the basis of the following criteria:

— each ray should cross the lower boundary of the study volume immediately under the block;

— the lower point of the ray should be above the core-mantle boundary;

— each earthquake should be recorded by at least 50 stations within a certain interval of epicentral distances (from 24° to 93°);

— each station should record at least 20–40 earthquakes;

— only shallow earthquakes (<30 km) should be used to exclude the sources within the target depth interval, and because the source parameters of shallow earthquakes can be better constrained.

Earthquake magnitudes were not taken into account, but the earthquakes that meet these conditions should obviously be strong enough.

The 3D modeling was based on the 1D standard global reference model PEM-A [39]. However, the choice of reference velocity pattern in teleseismics causes no critical influence on the final results. Details of the computing procedure are given in [37]. The main idea consists in successive averaging of residuals for each source and for each station in each block. The final residuals correspond to the following conditions:

$$\sum_{r=1}^{n} \delta t_{rs} = 0, \quad s = 1, ..., M,$$

$$\sum_{s=1}^{m} \delta t_{rs} = 0, \quad r = 1, ..., N,$$

where n is the number of receivers that record the s-th source, m is the number of sources recorded by the r-th receiver, M and N are the total numbers of sources and receivers, correspondingly.

To allow for the nonuniform distribution of sources and receivers, computation was made for composite rays with average characteristics which stand for a number of rays having similar paths. The averaging intervals were as follows:

— size of a cell on the surface from 30 to 50 km;
— epicentral distances from 10° to 15°;
— azimuths from 10° to 20°.

PARAMETERIZATION AND INVERSION ALGORITHM

3D velocity distribution is described by the Vertex parameterization method [36, 37] in which velocity anomalies are computed in grid nodes. The nodes are arranged according to the density of composite rays. The study volume is divided into tetrahedral cells with vertices coinciding with the parameterization nodes. The constant velocity gradient inside each tetrahedron provides continuous velocity distribution. Each node has its influence area within the adjacent tetrahedrons. The first derivative matrix is computed on the basis of rays traced in the reference model. Denote the elementary segment of the i-th ray as ΔS. The elementary delay at this segment due to velocity variation in the j-th node is computed as:

$$dt_i = - dV_j (S)\, \Delta S/V^2,$$

where V is the average velocity in a point of the ray, dV_j is the velocity variation at the point of the ray related to the elementary velocity variation in the j-th node. The influence of each node is integrated along the i-th ray and divided by the velocity variation in the j-th node. The integration along the ray path gives the A_{ij} element of the first derivative matrix.

This matrix differs from other similar matrices obtained in common 3D parameterizations, as it is (i) more densely packed because each point on the ray is "controlled" by several nodes rather than one block, and (ii) more uniformly filled (both in lines and in columns), as each node "controls" roughly equal numbers of rays. Therefore, this matrix is more stable, which is especially important in the case of noisy data. Inversion using this scheme can be stable even when noise exceeds the relevant signal [36].

The matrix inversion was based on the LSQR method [40, 41], which provides fast solution of large linear systems using the least computer resources. To check this method, LSQR and SVD inversion techniques were applied to a number of blocks, and comparison of the results showed a satisfactory correlation.

An analysis of the sparse inversion results showed that the coherent signal produced by anomalies in the study volume made only 10–15% of the residuals. Thus, a considerable portion of residuals in our data is related to random noise and external anomalies. Nevertheless, as shown by some tests presented below, the position of major patterns is stable, though there is a problem of reliability of the computed amplitude of the anomalies, which is sensitive to variations of sparse inversion parameters (number of iterations in LSQR or of singular numbers in SVD). With the noise we have, it is extremely difficult to choose the appropriate criteria of the optimum inversion parameters in search for realistic amplitudes.

RESULTS

The P-wave velocity structure at depths from 100 to 500 km beneath the Alpine-Himalayan orogen obtained using the ITS inversion is presented in Figures 4–8. The maps result from summation of models for sixty separate overlapping blocks (Fig. 3).

It appears appropriate to test the stability of our results before proceeding to their interpretation, as the initial data are too noisy. The reliability of the results and the resolution of our model in different parts of the study region were checked by several tests.

As mentioned above, ITS may be sensitive to epicentral errors. For example, a 20 km shift to the east may result into 2 sec longer travel times of rays coming from the west and 2 sec shorter travel times for the rays from the east. However, even such mislocation, which is random, can be separated from the coherent signal of anomalies if the number of sources is large enough. In the first test, sources were shifted arbitrarily to distances from 0 to 50 km (20 km in average) from their initial position according to the ISC bulletin. This error is much greater than any that might be expected for the real location of sources we dealt with. The results of inversion for the original (on the left) and shifted (on the right) sources at depths of 200 and 400 km are shown in Figure 9. At the depth of 200 km the difference mostly is in the amplitude of anomalies, apparently related to instability caused by high random noise, while the position of major anomalies is rather stable, and rather good correlation is achieved at 400 km. Therefore, mislocation does not disturb much the final results and is more strongly pronounced at shallower depths.

In the second test, data were arbitrarily divided into two equal groups and earthquakes were assigned odd and even numbers. The results of inversion (Fig. 10) are shown for the total data set (*a*) and separately for even (*b*) and odd (*c*) sources. Comparison of the maps shows whether the anomalies are reliable and independent from random effects. The resolution of our model, estimated also from this test, is at least 100–150 km.

The third test shows the ability of the method to reconstruct certain synthetic anomalies. For this test we chose Southern Siberia and Mongolia (Fig. 11), though it is not the best region in terms of ray coverage and data quality. The initial synthetic model is shown in the left top map. The negative anomalies evident at all depths are assumed to model a mantle plume. Two high-velocity anomalies between 100 and 300 km simulate lithospheric thickening. Residuals have been computed from tracing of actual rays through these anomalies and were then added with random noise of the same magnitude as the relevant signal. After that the data were inverted following the complete procedure. The least stability and greatest deviation from the model is at 100 km, and the results in other sections are quite satisfactory. This test highlights the problem of low vertical resolution inherent to all teleseismic schemes, namely that the maps cannot reliably constrain the bottom of thick lithosphere, though provide a quite precise plan view of the anomalies. Therefore, the high-velocity patterns interpreted as traces of lithosphere that penetrated into the mantle may in reality be not so deep as we might expect from our models.

In addition to these three, some more tests were applied to check the stability of the results and the algorithm, namely:

— test for reproducibility of anomalies in block overlaps;

— fitting of number of nodes in the parameterization grid;

— fitting of parameterization grid types (nodes and blocks, with constant and variable density of nodes, grids with various spatial orientations, etc.);

— fitting block sizes;

— “checkerboard test”

All tests showed that most patterns presented in maps 4–8 are regular and bear low random noise.

DISCUSSION

A number of elongate positive anomalies in Figs. 4, 6, and 7 are interpreted as traces of lithosphere that penetrated into the mantle. The probable position of the slabs (shown by a light-color dashed line on horizontal sections) was outlined proceeding from high-velocity patterns, distribution of deep seismicity (Fig. 2), and geological evidence.

Traces of the Africa-Europe collision are well evident in the western part of the region (Fig. 4). A strong positive anomaly persists at all depths beneath the Apennines and can be reliably attributed to a sinking slab, marked also by deep seismicity to depths below 200 km. However, as the slab is located on the periphery of the study region, the details of its geometry are poorly resolved.

Moving east along the Adriatic sea and the Mediterranean, one can follow the subduction zone of the African plate beneath the Dinarides and the Cretan arc. In the upper layers, the anomaly corresponding to the African slab, has a rounded shape following the Cretan arc, and in the lower part it grades into an isometric feature beneath the Aegean Sea and the Bosphorus and Dardanelles straits. The position of the slab is also distinctly traced by deep earthquake sources on the vertical sections. A similar setting was reported in other studies [24–26]. Note that negative anomalies beneath the central Aegean Sea are restricted to the upper 200 km. This explains the Late Cenozoic magmatism in this region [42] as a result of extension of the Aegean plate that caused the rise of asthenospheric material [4] rather than a consequence of mantle plume activity.

A much more complicated setting occurs east of the Cretan arc. Our maps depict a series of high-velocity anomalies extending as far as the Caucasus. (Note that these anomalies are worse resolved in the tomography

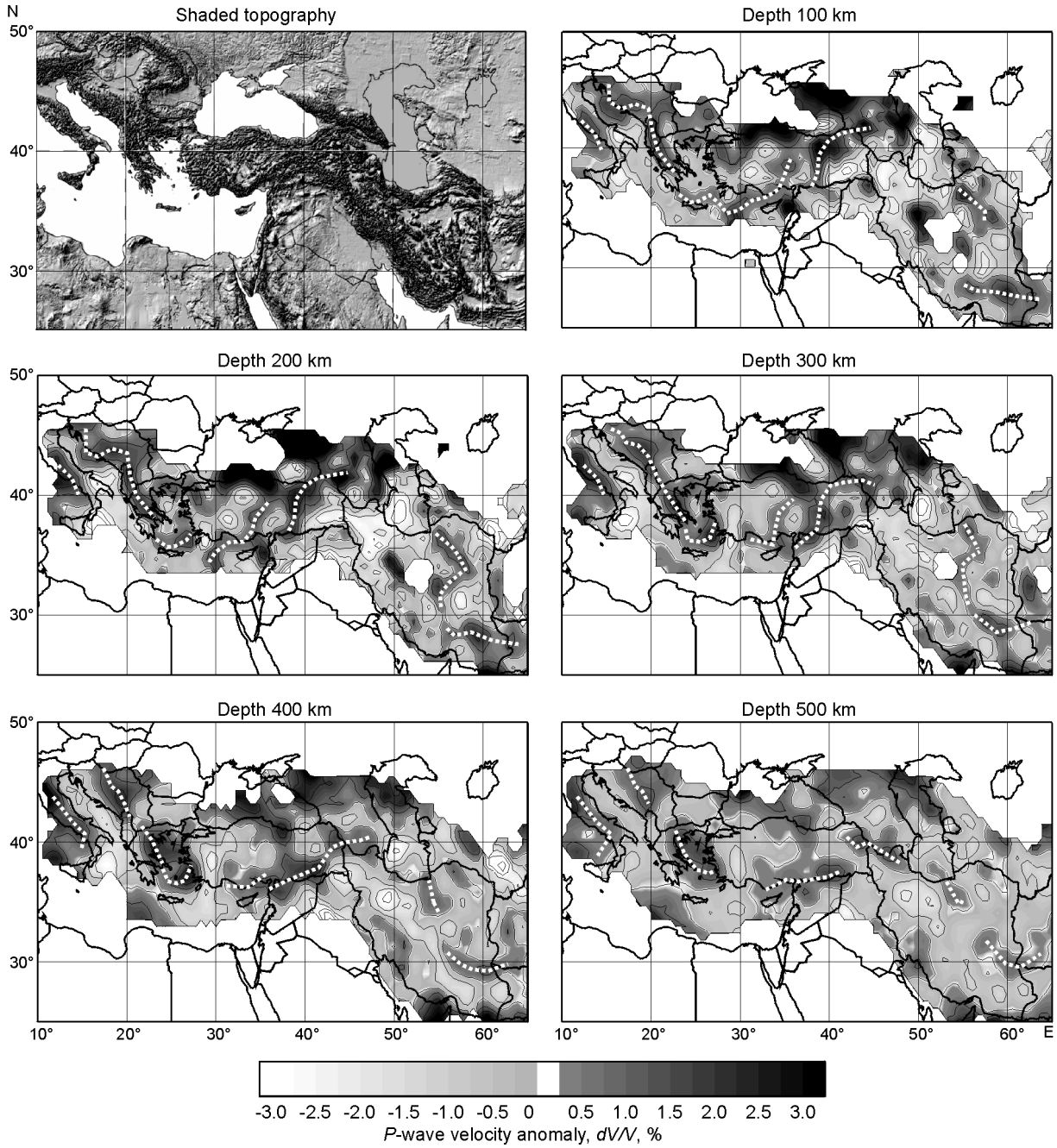

Fig. 4. *P*-wave velocity anomalies beneath two western segments of Alpine-Himalayan orogen, horizontal sections. Dark color indicates high velocities. Contour interval is 1%. Hypothetical position of slabs and lithospheric thickening are shown by light-color dashed lines.

studies cited earlier.) These anomalies may trace subduction — though not so clearly as those of the Dinarides and the Cretan arc — which is also indicated by high-seismicity belts along the anomalies. Vertical sections B1—B2 and C1—C2 show at least two differently oriented slabs in this zone. A sinking slab steeply dips northward near Cyprus, and another slab is oriented in the opposite direction in eastern Turkey. The upper part of the latter slab is much thicker than the lower one (see section C1—C2). This may be evidence of transition from oceanic to continental subduction. A strong shallow positive anomaly in the north of the region is associated with the Anatolian fault that separates the Turkish and Black Sea plates. It currently acts as a typical left-lateral strike-slip

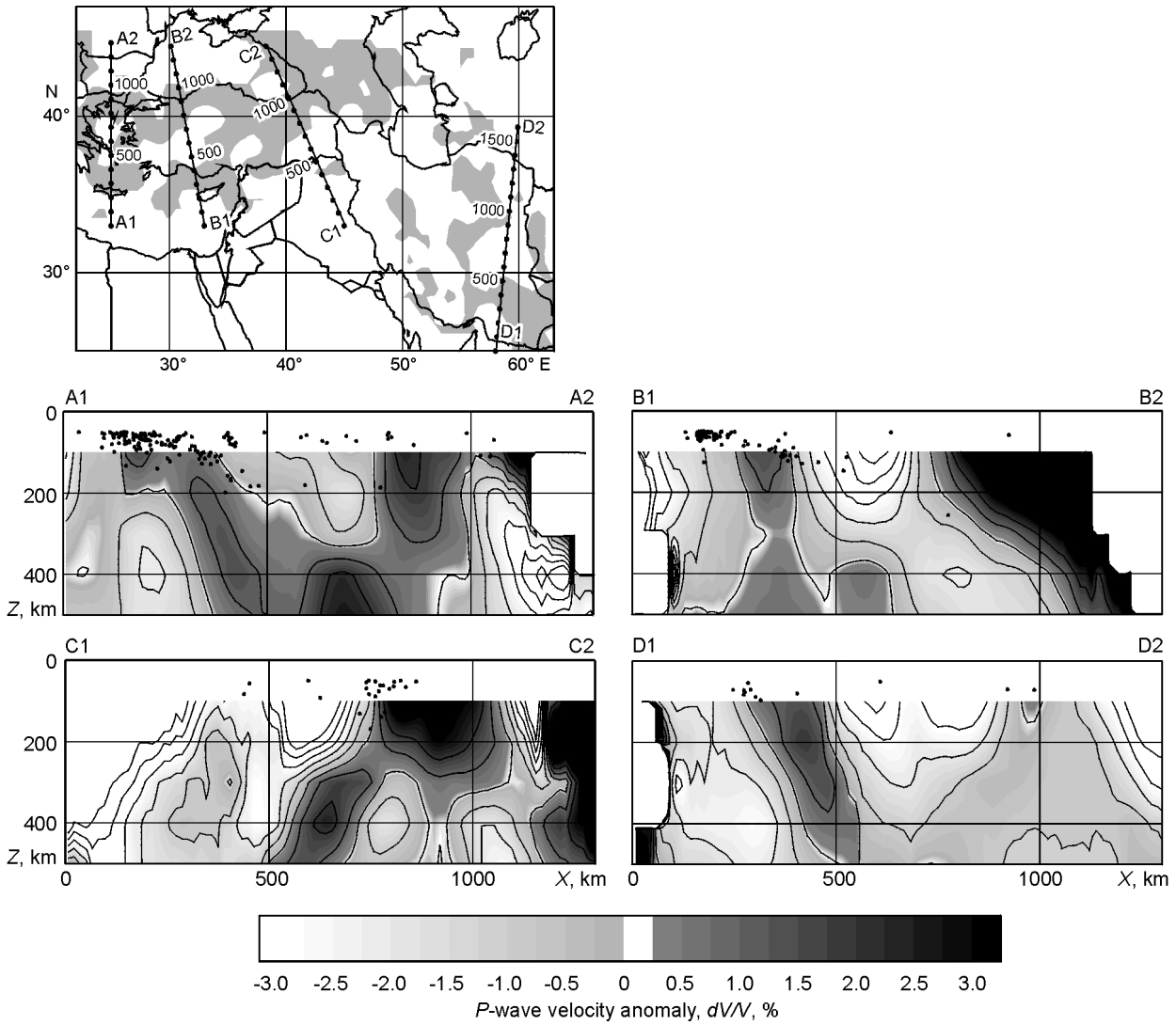

Fig. 5. Vertical sections of *P*-wave velocity anomalies along four profiles in two western segments of Alpine-Himalayan orogen. Dark color indicates high velocities. Contour interval is 1%. Black dots show locations of deep earthquakes (>50 km) in a 50 km wide strip along profile. Position of profiles is indicated on map above. Dark areas show positive seismic anomalies at 200 km.

fault, and strike-slip faulting in the recent past may have caused partial sinking of the lithosphere. This setting would be consistent with the general compression regime observed throughout the orogen.

The structure of the orogen segment from Turkey to Iran is not so clear as in the western segment. Traces of subduction in the region of Zagros are almost invisible, though high deep seismicity is evident there. Apparently, subduction, if any, is actually at its inception, and the amount of lithospheric material accumulated in the upper mantle is beyond the detection limit of seismic tomography. At the same time, the traces of collision in the Caucasus, Kopet Dagh and Lut (section D1—D2) are clearly seen. The high-velocity anomaly agrees with the distribution of deep-focus earthquakes and coincides with the position of the Triassic subduction zone [12]. The collision traces look as different structures at shallow depths, but according to their shapes at deeper sections, they may be linked into a single subduction zone that might have dispersed in recent time because of the transition from oceanic to continental subduction.

The pattern of the Pliocene-Quaternary volcanism in the Persian block south of the Caspian Sea [10] corresponds to large low-velocity anomalies at depths down to 400 km. Our results suggest that this volcanic activity may have been associated with the anomalous heating of the upper mantle.

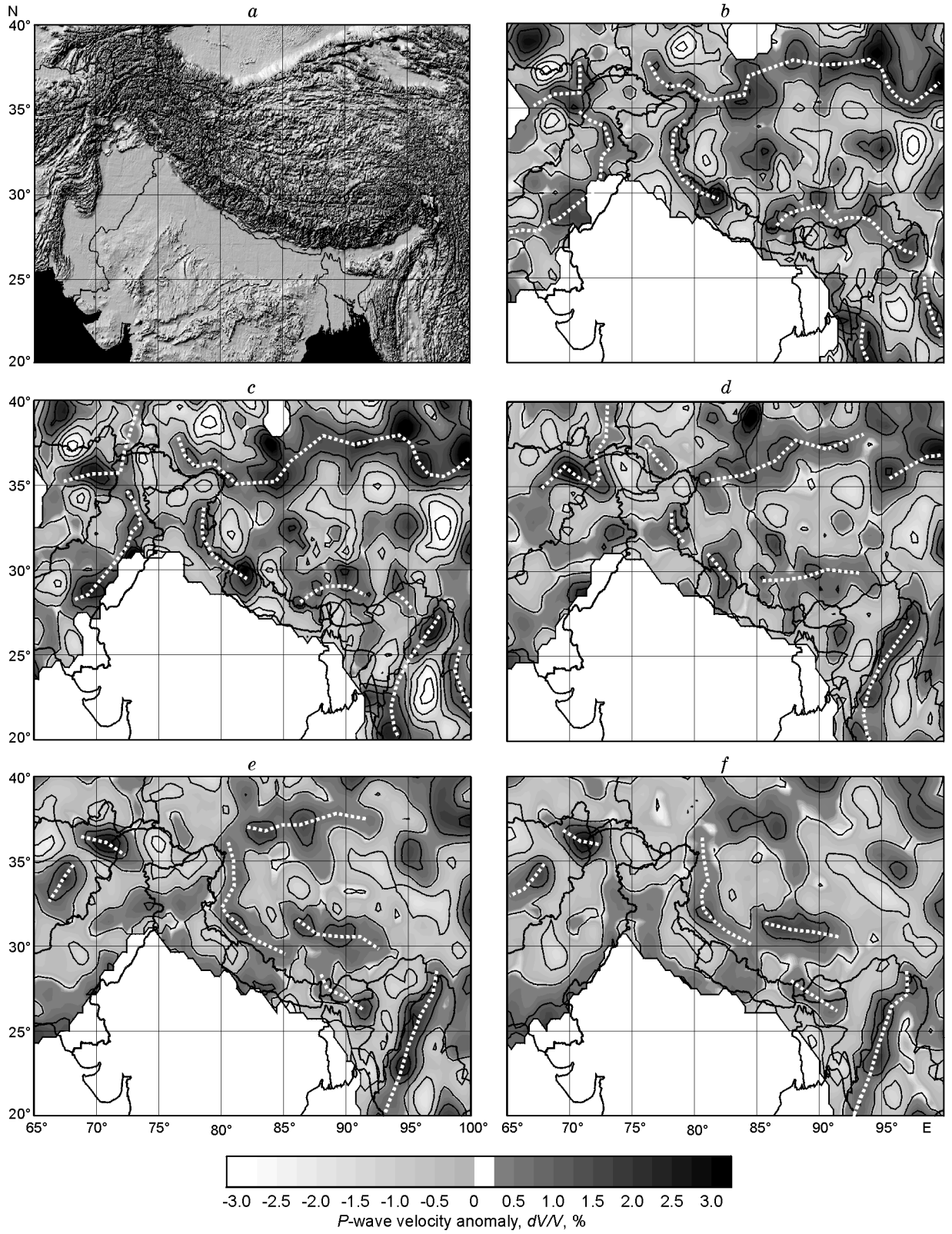

Fig. 6. *P*-wave velocity anomalies beneath central segment of Alpine-Himalayan orogen, horizontal sections. *a* — Surface topography of study area, *b–f* — velocity structure at different depths (km): 100 (*b*), 200 (*c*), 300 (d), 400 (*e*), 500 (*f*). Dark color indicates high velocities. Contour interval is 1%. Hypothetical position of slabs and lithospheric thickening are shown by light-color dashed lines.

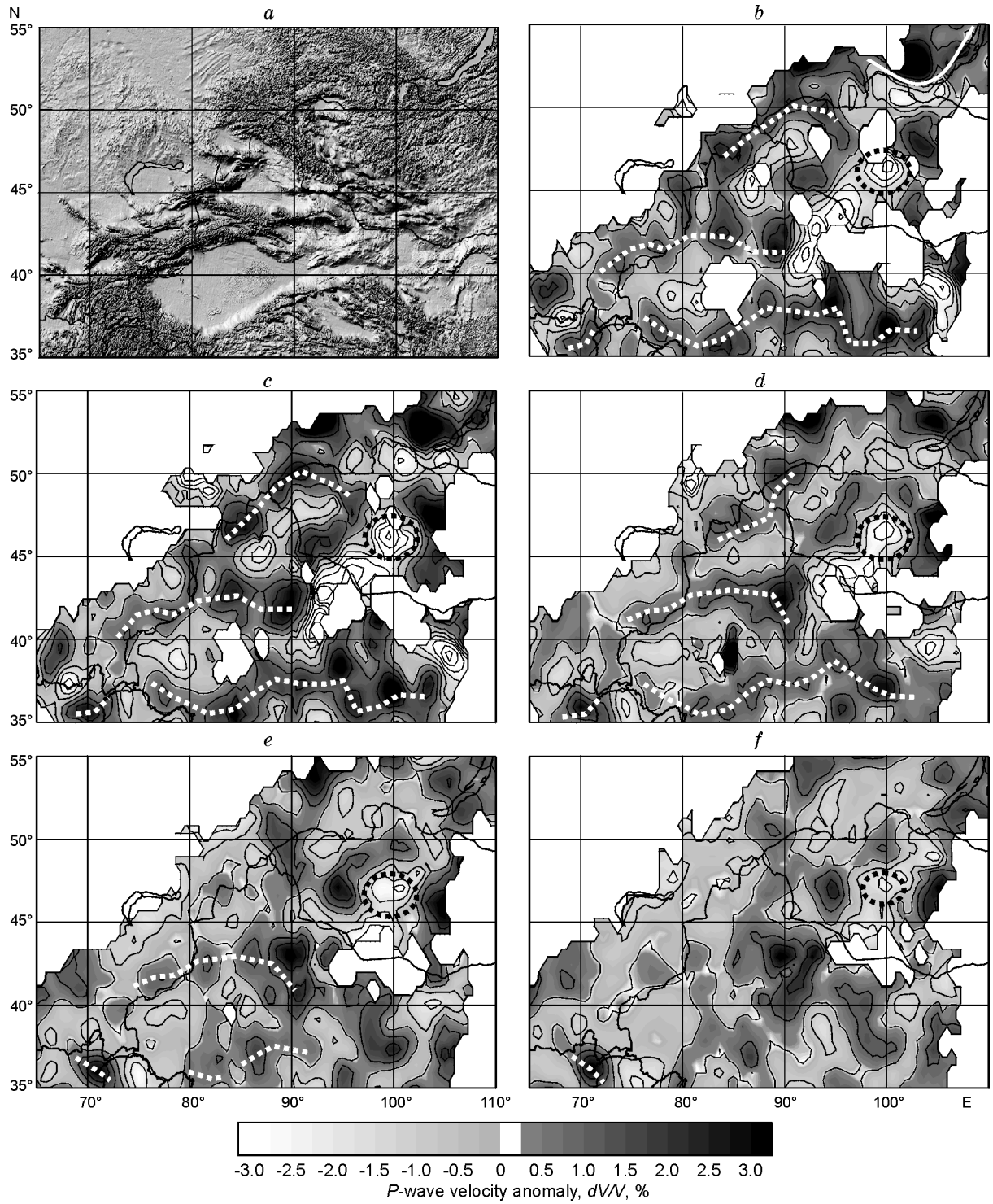

Fig. 7. *P*-wave velocity anomalies beneath eastern segment of Alpine-Himalayan orogen, horizontal sections. Legend same as in Fig. 6.

The structure of the upper mantle beneath the third segment including Hindukush and Tibet is shown in Fig. 6. The nearly vertical high-velocity anomaly beneath the Hindukush and Pamir mountains (section A1—A2, Fig. 8) can be unambiguously attributed to a subducted slab, which is confirmed by strong deep seismicity to a

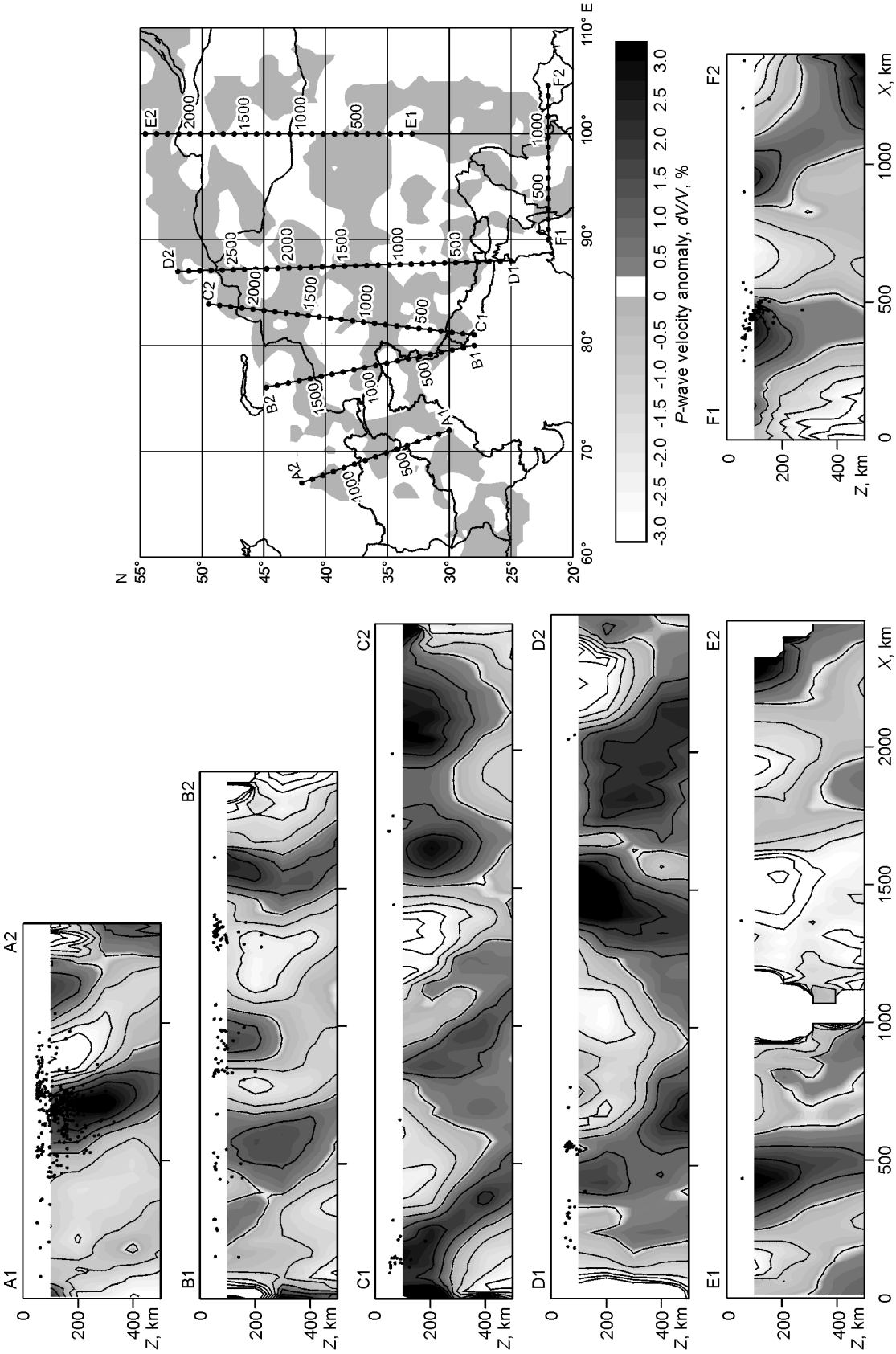

Fig. 8. Vertical sections of *P*-wave velocity anomalies along six profiles in eastern segment of Alpine-Himalayan orogen. Dark color indicates high velocities. Contour interval is 1%. Black dots show locations of deep earthquakes (>50 km) in a 50 km wide strip along profile. Position of profiles is indicated on map (right top). Dark areas show positive seismic anomalies at 200 km.

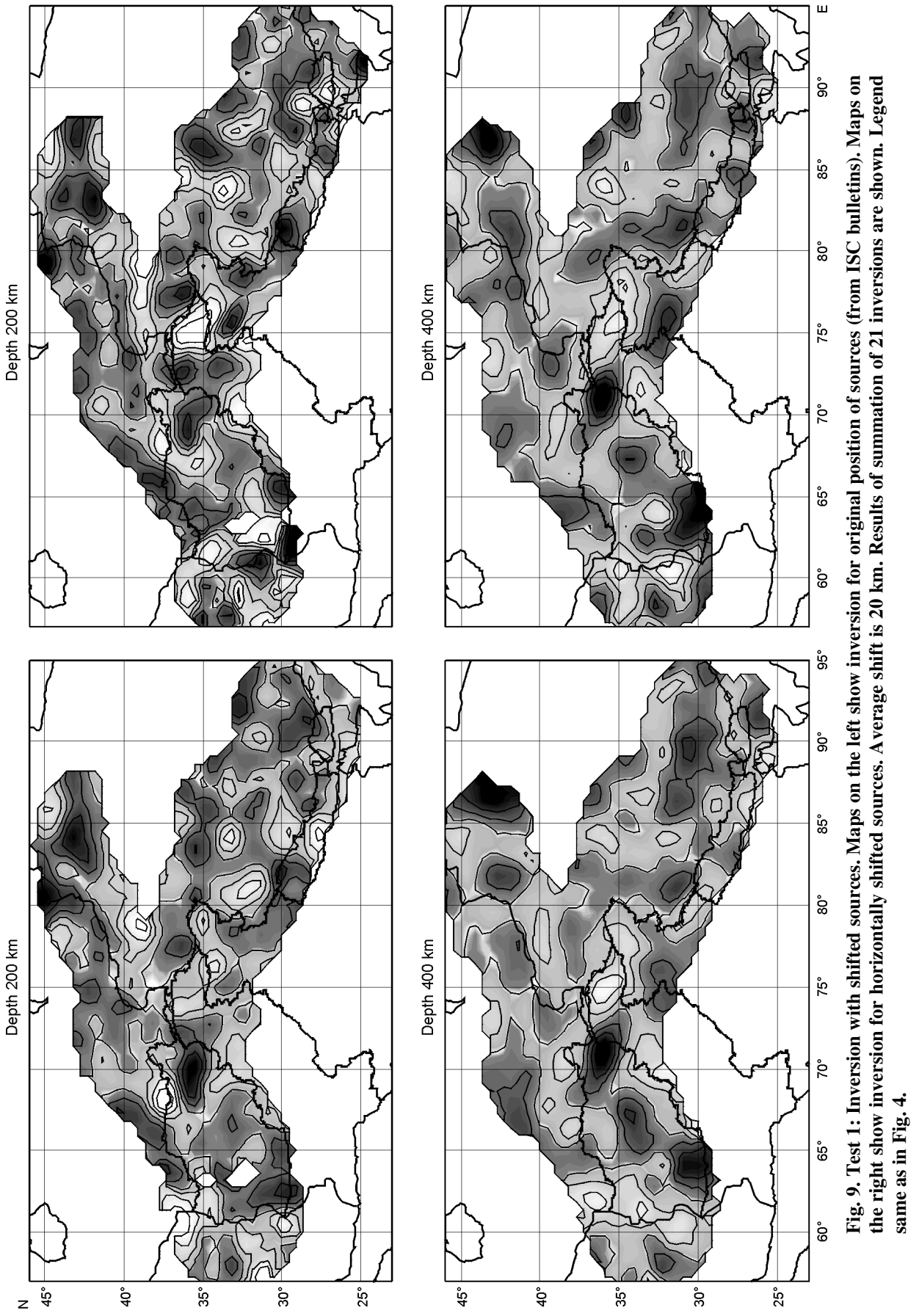

Fig. 9. Test 1: Inversion with shifted sources. Maps on the left show inversion for original position of sources (from ISC bulletins). Maps on the right show inversion for horizontally shifted sources. Average shift is 20 km. Results of summation of 21 inversions are shown. Legend same as in Fig. 4.

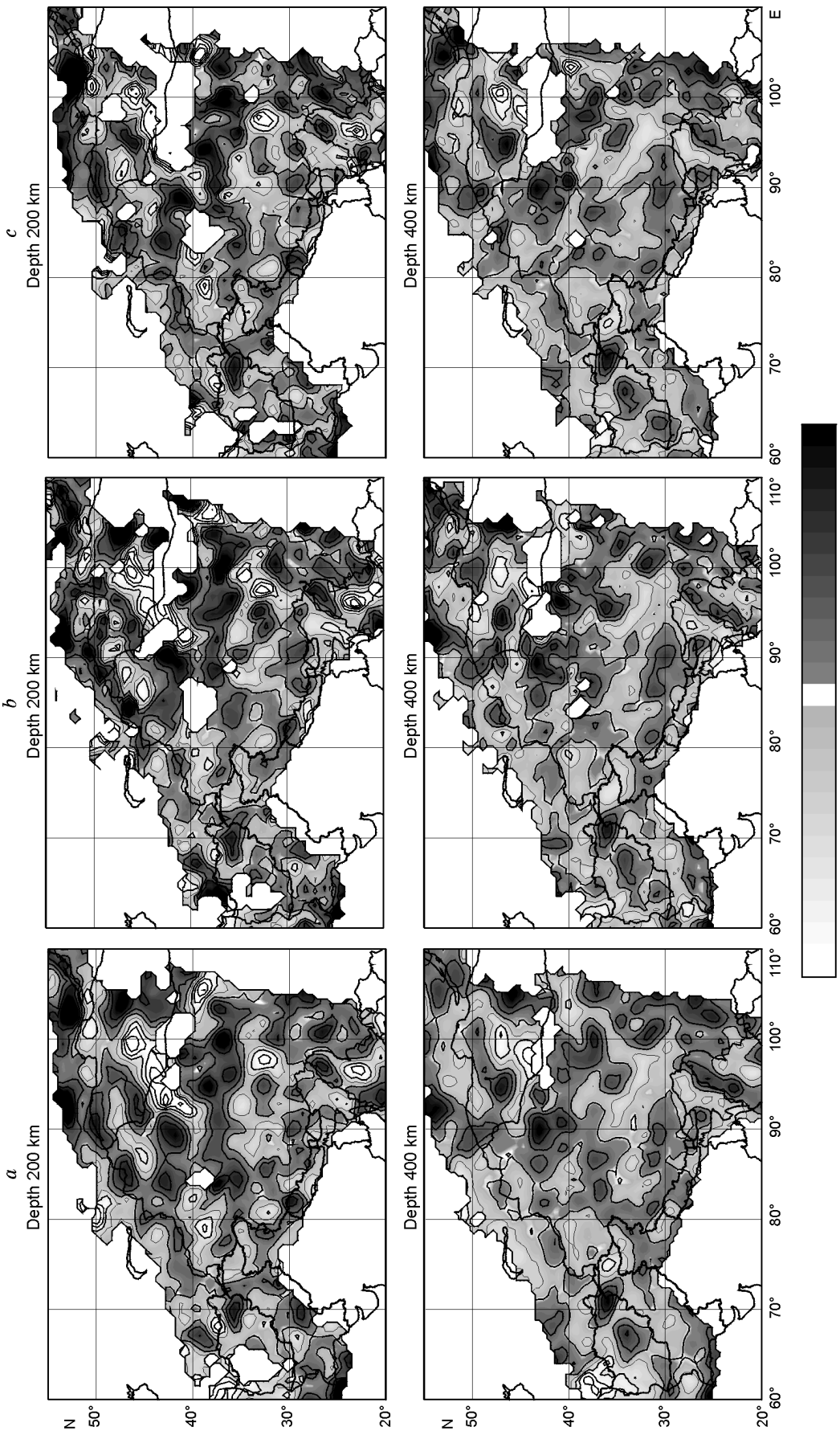

Fig. 10. Test 2: Inversion of independent datasets. Maps on the left show inversion of all data, maps in the middle show inversion for odd-number earthquakes, maps on the right show inversion for even-number earthquakes. *a* — All data, *b* — even-number earthquakes, *c* — odd-number earthquakes. Legend same as in Fig. 4.

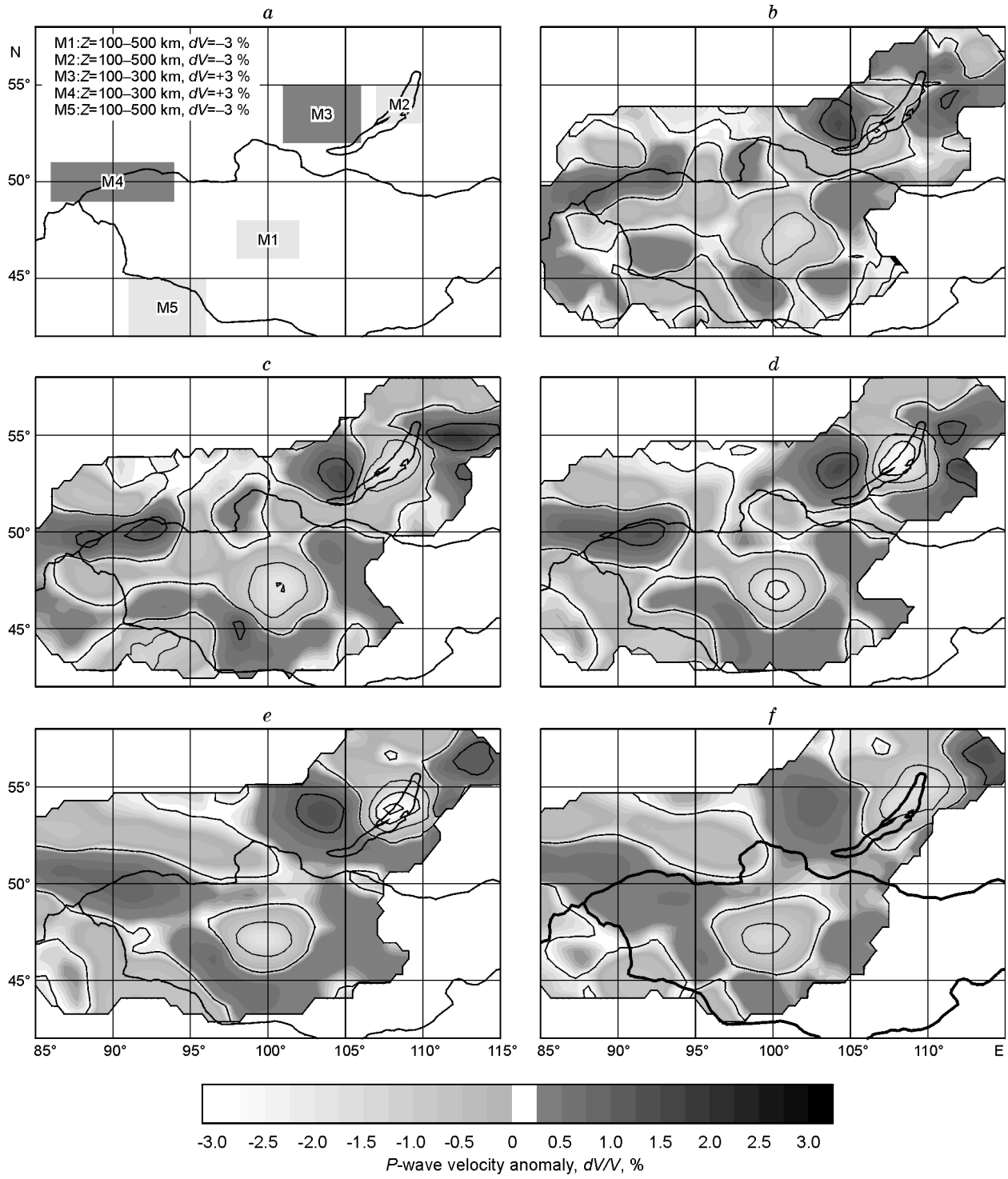

Fig. 11. Test 3: Recovery of synthetic anomalies. *a* — Initial synthetic model; *b–f* — results of inversion at different depths: 100 km (*b*), 200 km (*c*), 300 km (*d*), 400 km (*e*), 500 km (*f*). Legend same as in Fig. 4.

depth of 500 km. The Burma slab is well defined in the southeastern margin of the segment (section F1—F2, Fig. 8). Subduction zones elsewhere within this segment are rather hypothetical.

A series of elongate high-velocity anomalies is traceable along the Himalayas and is broken in the central part of Nepal. According to their shapes at different depths, the anomalies may be interpreted as traces of several

slabs, at least within the studied depth range. Such complex behavior of subduction in this collision zone must be related to high inhomogeneity of the lithosphere consisting of rigid continental blocks, orogenic belts, and thin oceanic plates. The velocity structure beneath the Himalayas and Tibet is also presented in the southern part of three vertical sections (B1—B2, C1—C2, and D2—D2) in Fig. 8.

Note that low-velocity anomalies predominate beneath Tibet. A distinct low beneath Kunlun (93° E, 35° N) is consistent with the regional teleseismic tomography images from a temporary seismological network [33].

Seismic anomalies beneath the eastern segment of the orogen (Tarim, Tien Shan, southern Siberia and Mongolia) are shown in Fig. 7. Some surface structures demonstrate obvious correlation with deep patterns. For instance, the contours of the Tarim plate correspond to a negative anomaly which is traceable to a depth of 100–300 km and is surrounded by linear high-velocity anomalies in the south and in the north. The same is the situation for the Jonggar plate. Therefore, active deformation of relatively weak material can be inferred between several rigid blocks (Kazakh shield, Tarim and Jonggar plates), as well as shortening at the expense of this weak lithosphere sinking to the upper mantle under the pressure from the Indian plate. The Tibet plate is subducted under Tarim from the south (see section C1—C2 in Fig. 8); the direction of subduction north of Tarim is uncertain. Judging from the rate of convergence of the Tarim plate and the Kazakh shield (about 2 cm/year, from GPS data [43]), at least 400 km of lithosphere must have subducted for the past 20 myr. The positive anomaly in the upper mantle between the Tarim basin and the Kazakh shield may be related to weak lithosphere squeezed down by the converging rigid blocks.

The negative anomalies beneath the Tarim basin and other rigid blocks are not necessarily the evidence of anomalous heating. They may appear in contrast to strong highs produced by sinking lithosphere around the blocks and are related to the specificity of the inversion techniques we used.

Note that the linear structures of Mongolian Altai have no correspondence to deep seismic patterns. Therefore, the processes responsible for mountain building in this region are of shallow origin. At the same time, a strong isometric velocity low in Mongolia coincides with the Hangayn plateau (Fig. 7, dark dashed line). The existence of a gravity anomaly and recent volcanism allows us to associate this anomaly with a mantle plume that played a role in the development of Central Asia. The shape of the plume is also traceable in vertical section E1—E2.

The outlines of the Siberian craton near Lake Baikal are expressed in the shallowest horizontal sections (Fig. 7) as a strong positive anomaly surrounded by low-velocity patterns. However, there is no evidence of a mantle plume which could cause active rifting in this region.

CONCLUSIONS

The Inversion Teleseismic Scheme can provide high-resolution images of the upper mantle structure under active seismic regions. The research can be performed on the basis of open-file ISC bulletin data. Inversion for separate blocks, which is an equivalent of high-frequency data filtering, allows detecting subtler anomalies than the global tomography. However, these results cannot be used in estimates of absolute velocities.

The test in which events are grouped as odd and even numbers is more helpful in showing the stability of the obtained patterns than the sensitivity test. In contrast to the latter, which shows the theoretical stability of the method with respect to the fixed size of anomalies, our test also accounts for the quality of initial data.

The seismic structure beneath the Alpine-Himalayan orogenic belt shows that subduction is possible in continental settings as well, as a result of strong plate collisions. Slabs that clearly indicate the existence of subduction are best evident in the regions of Apennines, Dinarides, Hellenides, Cretan arc, Hindukush, Pamirs, and western Indo-China. In other regions the traces of these slabs are shown by tomography but are less distinctly pronounced as classical subduction zones. They may image continental lithosphere penetrated down to 400 km due to regional compression, as it occurs in the Caucasus, Tien Shan, Himalayas, Kunlun, and Tibet.

The obtained results indicate plume traces in different places of Eurasia, including one beneath the Hangayn dome in Mongolia, which is consistent with other geophysical evidence.

REFERENCES

1. Dewey, J.F., W.C. Pitman, B.F.Ryan, and J. Bonnin, Plate tectonics and the evolution of the Alpine system, *Geol. Soc. Amer. Bull.*, **84**, 3137–3180, 1973.

2. Sborshchikov, I.M., V.I. Dronov, S.M. Kalumulin, and S.Kh. Mirzod, Structural relationship between the Tura plate and the Alpine orogens, *Geotektonika*, 104–105, 1974.

3. Nowroozi, A.A., Focal mechanism of earthquakes in Persia, Turkey, Pakistan and Afghanistan and plate tectonics in the Middle East, *Bull. Seismol. Soc. Am.*, **62**, 823–850, 1972.

4. McKenzie, D., Active tectonics of the Mediterranean region, *Geophys. J. R. Astr. Soc.*, **30**, 109–185, 1974.

5. Zonenshain, L.P., and L.A. Savostin, *Introduction into geodynamics* [in Russian], 311 pp., Nedra, Moscow, 1979.

6. Trifonov, V.G., *Neotectonics of Asia* [in Russian], 252 pp., Nauchny Mir, Moscow, 1999.

7. Dercourt, J., L.P. Zonenshain, L.-R. Ricou, V.G. Kazmin, X. Le Pichon, A.L. Knipper, C. Grandjacquet, I.M. Sbortshikov, J. Geyssant, C.Levrier, D.M. Pechersky, J. Boulin, J.-C. Sibuet, L.A. Savostin, O. Sorokhtin, M. Westphal, M.L. Bazhenov, J.P. Lauer, and B. Biju-Duval, Geological evolution of the Tethys from the Atlantic to the Pamir since the Lias, *Tectonophysics*, **123**, 241–315, 1986.

8. Gealey, W.K., Plate tectonic evolution of the Mediterranean-Middle East region, *Tectonophysics*, **155**, 285–306, 1988.

9. Morgan, W.J., Convection plumes in the lower mantle, *Nature*, **230**, 42–43, 1971.

10. Sengör, A.M.C., and W.S.E. Kidd, Post-collisional tectonics of the Turkish-Iranian plateau and a comparison with Tibet, *Tectonophysics*, **55**, 361–376, 1979.

11. Tapponnier, P., M. Mattauer, F. Proust, and C. Cassaigneau, Mesozoic ophiolites and large scale tectonic movements in Afghanistan, *Earth Planet. Sci. Lett.*, **52**, 355–371, 1981.

12. Kaz'min, V.G., and A.L. Knipper, Accretionary tectonics of the Caucasus, in *Tectonic processes* [in Russian], ed. Yu.M. Pushcharovsky and A.A. Mossakovsky, 75–89, Nauka, Moscow, 1989.

13. Klootwijk, C.T., J.S. Gee, H.W. Peirce, G.M. Smith, and P.L. McFadden, An early India-Asia contact: Paleomagnetic constraints from Ninetyeast Ridge, ODP Leg 121, *Geology*, **20**, 395–398, 1992.

14. Windley, B.F., M.B. Allen, C. Zhang, Z.-Y. Zhao, and G.-R. Wang, Paleozoic accretion and Cenozoic redeformation of the Chinese Tien Shan range, Central Asia, *Geology*, **18**, 128–131, 1990.

15. Dewey, J.F., R.M. Shackleton, C. Chang, and Y. Sun, The tectonic evolution of the Tibetan Plateau, *Philos. Trans. R. Soc. London*, **A 327**, 379–413, 1988.

16. Molnar P., and P. Tapponnier, Cenozoic tectonics of Asia: Effects of a continental collision, *Science*, **189**, 419–426, 1975.

17. Dobretsov, N.L., N.A. Berzin, M.M. Buslov, and V.D. Ermikov, General aspects of the evolution of the Altai region and the interrelationships between its basement pattern and the neotectonic structural development, *Geologiya i Geofizika (Russian Geology and Geophysics)*, **36**, 10, 5–19(3–15), 1995.

18. Dobretsov, N.L., M.M. Buslov, D. Delvaux, N.A. Berzin, and V.D. Ermikov, Meso- and Cenozoic tectonics of the Central Asian mountain belt: Effects of the lithospheric plates interaction and mantle plumes, *Intern. Geol. Rev.*, **38**, 430–466, 1996.

19. Yarmolyuk, V.V., V.I. Kovalenko, and M.I. Kuz'min, The North Asian plume in the Phanerozoic: Magmatism and deep-seated geodynamics, *Geotectonics*, **5**, 3–29, 2000.

20. Zhang, Y.-S., and T. Tanimoto, High resolution global upper mantle structure and plate tectonics, *J. Geophys. Res.*, **98**, 9793–9823, 1993.

21. Su, W.-J., R.L. Woodward, and A.M. Dziewonski, Degree 12 model of shear velocity heterogeneity in the mantle, *J. Geophys. Res.*, **99**, 6945–6980, 1994.

22. Grand, S.P., R.D. van der Hilst, and S. Widiyantoro, Global seismic tomography: A snapshot of convection in the Earth, *GSA Today*, **7**, 1–7, 1997.

23. Van der Hilst, R.D., S. Widiyantoro, and E.R. Engdahl, Evidence for deep mantle circulation from global tomography, *Nature*, **186**, 578–584, 1997.

24. Bijwaard, H., W. Spakman, and E.R. Engdahl, Closing gap between regional and global travel time tomography, *J. Geophys. Res.*, **103**, 30,055–30,078, 1998.

25. Spakman, W., S. van der Lee, and R.D. van der Hilst, Travel time tomography of the European-Mediterranean mantle down to 1400 km, *Phys. Earth Planet. Inter.*, **79**, 3–74, 1993.

26. Piromallo, C., and A. Morelli, Imaging the upper mantle by P-wave travel time tomography, *Ann. Geophysica*, **40**, 963–979, 1997.

27. Roecker, S.W., Tomography in zones of collision: Practical considerations and examples, in *Seismic tomography, theory and practice*, ed. H.M. Iyer and K. Hirahara, 584–612, Chapman and Hall, London, 1993.

28. Mohan, G., and S.S. Rai, Large-scale three-dimensional seismic tomography of the Zagros and Pamir-Hindukush regions, *Tectonophysics*, **242**, 255–265, 1995.

29. Romanowicz, B., Constraints on the structure of the Tibet plateau from pure phase velocities of Love and Rayleigh waves, *J. Geophys. Res.*, **87**, 6865–6883, 1982.

30. Bourjot, L, and B. Romanowicz, Crust and upper mantle tomography in Tibet using surface waves, *Geophys. Res. Lett.*, **19**, 881–884, 1992.

31. Holt, W.E., and T.C. Wallance, Crustal thickness and upper mantle velocities in the Tibetan plateau

region from the inversion of regional P_{ni} waveforms: Evidence for a thick upper mantle lid beneath southern Tibet, *J. Geophys. Res.*, **95**, 12,499–12,525, 1990.

32. McNamara, D.E., W.R. Walter, T.J. Owens, and C.J. Ammon, Upper mantle velocity structure beneath the Tibetan plateau from P_n tomography, *J. Geophys. Res.*, **102**, 493–505, 1997.

33. Witlinger, G., F. Masson, G. Poupinet, P. Tapponnier, J. Mei, G. Herquel, J. Guilbert, U. Achauer, X. Guanqui, Shi Danian, and Lithoscope Kunlun Team, Seismic tomography of northern Tibet and Kunlun: evidence for crustal blocks and mantle velocity contrasts, *Earth Planet. Sci. Lett.*, **139**, 263–279, 1996.

34. Woodward, R.L. and R. Molnar, Lateral heterogeneity in the upper mantle and *SS-S* traveltime interval for *SS* rays reflected from the Tibetan Plateau and its surroundings, *Earth Planet. Sci. Lett.*, **135**, 139–148, 1995.

35. Liu, F., and A. Jin, Seismic tomography of China, in: *Seismic tomography, theory and practice*, ed. H.M. Iyer and K. Hirahara, 299–318, Chapman and Hall, London, 1993.

36. Kulakov, I.Yu., S.A. Tychkov, and S.I. Keselman, Three-dimensional structure of lateral heterogeneities in *P* velocities in the upper mantle of the southern margin of Siberia and its preliminary geodynamic interpretation, *Tectonophysics,* **241**, 239–257, 1995.

37. Koulakov, I.Yu., 3D tomographic structure of the upper mantle beneath the central part of Eurasian continent, *Geophys. Journ. Intern.*, **133**, 467–489, 1998.

38. Petit, C., I. Koulakov, and J. Déverchère, Velocity structure around the Baikal rift from teleseismic and local earthquake traveltimes and geodynamic implications, *Tectonophysics*, **296**, 125–144, 1998.

39. Dziewonski, A.M., A.L. Hales, and E.R. Lapwood, Parametrically simple earth models consistent with geophysical data, *Phys. Earth Planet. Inter.*, **10**, 12–48, 1975.

40. Paige, C.C., and M.A. Saunders, LSQR: An algorithm for sparse linear equations and sparse least squares, *ACM Trans. Math. Soft.*, **8**, 43–71, 1982.

41. Van der Sluis, A., and H.A. van der Vorst, Numerical solution of large, sparse linear algebraic systems arising from tomographic problems, in *Seismic tomography,* ed. G. Nolet, 49–83, Reidel, Dortrecht, 1987.

42. McKenzie, D., and R.K. O'Nions, The source regions of ocean island basalts, *J. Petrol.*, **36**, 133–159, 1995.

43. Bragin, V.D., V.Yu. Batalev, A.V. Zubovich, A.N. Lobanchenko, A.K. Rybin, Yu.A. Trapeznikov, and G.G. Shchelochkov, Signature of neotectonic movements in the geoelectric structure of the crust and seismicity distribution in the central Tien Shan, *Geologiya i Geofizika (Russian Geology and Geophysics)*, **42**, 10, 1610–1621(1527–1538), 2001.

Editorial responsibility: N.L. Dobretsov Received 3 July 2001